SmartBot

WILEY | SmartBot

RESEARCH ARTICLE OPEN ACCESS

Compact Manipulator With Flexible Parallel Mechanisms and Variable Stiffness for Keyhole Procedures

Changsheng Li[1,2,3] | Jinpeng Diao[1,3] | Chao Qian[1,3] | Xipeng Wu[1,3] | Hongliang Ren[4] | Lin Cao[5] | Xingguang Duan[1,2,3]

[1]School of Mechatronical Engineering, Beijing Institute of Technology, Beijing, China | [2]School of Medical Engineering, Beijing Institute of Technology, Zhuhai, Guangdong, China | [3]Key Laboratory of Biomimetic Robots and Systems, Beijing Institute of Technology, Ministry of Education, Beijing, China | [4]Department of Electronic Engineering, The Chinese University of Hong Kong, Hong Kong, China | [5]Department of Automatic Control and Systems Engineering, The University of Sheffield, Sheffield, UK

Correspondence: Xingguang Duan (duanstar@bit.edu.cn)

Received: 17 July 2025 | **Revised:** 9 October 2025 | **Accepted:** 19 October 2025

ABSTRACT

Keyhole procedures frequently necessitate passing instruments through narrow, elongated surgical channels, presenting a significant challenge in designing manipulators with compact structures and superior remote dexterity. In this work, we propose a novel 7 degrees-of-freedom variable stiffness dexterous surgical manipulator based on a flexible parallel mechanism. The manipulator has an outer diameter of 4.5 mm and is characterized by a hollow structure that incorporates a central channel measuring 1.8 mm. This design facilitates the integration of tool drives and sensors within the manipulator, enhancing its overall functionality. The kinematics and stiffness model of the flexible parallel mechanism are derived. Additionally, a prototype of the proposed manipulator is presented and evaluated through sufficient experiments. We performed a teleoperation test to characterize the model accuracy of the prototype, and the average error is approximately 0.49 mm. Furthermore, we conduct a series of experiments to verify the prototype's performance, including workspace, stiffness, and dexterous operation. The results confirm that the surgical manipulator demonstrates excellent performance in the challenging environment of keyhole procedures.

1 | Introduction

The keyhole procedure represents a significant advancement in minimally invasive surgery (MIS), offering substantial benefits over traditional open surgery including reduced trauma, diminished pain, and accelerated recovery [1–3]. This approach has found widespread application across various surgical disciplines such as laparoscopy, neurosurgery, and arthroscopy. However, the inherent constraints of keyhole procedures, characterized by confined operating spaces and complex anatomical environments, impose rigorous requirements on surgical instruments, necessitating compact dimensions, enhanced flexibility, and adjustable stiffness capabilities to ensure both safety and efficacy [4]. Conventional rigid surgical instruments, constrained by their limited degrees of freedom (DOFs) and inadequate flexibility, often prove insufficient for addressing the complexities of modern minimally invasive operations [5].

In response to these challenges, the field has witnessed growing interest in dexterous robotic manipulators for MIS applications [6–9]. Several architectural paradigms have emerged, each presenting distinct advantages and limitations. Rope-driven mechanisms [10] facilitate manipulator miniaturization through remote actuator placement [11–13] and offer limited stiffness modulation via tendon tension adjustment [14], though they contend with accuracy limitations stemming from transmission-related issues including backlash, friction, and elastic deformation [15, 16]. Continuum architectures encompassing concentric tube systems [17], snake-like joint mechanisms [18], and serial spacer disk configurations [19] deliver exceptional flexibility and demonstrate considerable safety merits in complex surgical settings [20, 21], yet their operational effectiveness is often constrained by substantial bending radii that restrict deployment in tightly confined spaces [22, 23]. Linkage mechanisms provide expansive workspaces and

relatively straightforward control [24], but encounter significant obstacles in achieving both miniaturization and dexterity due to challenges associated with microscopic kinematic pair implementation [25]. Parallel mechanisms deliver superior precision, robust load capacity, and enhanced stability [26–28], though their adaptation to constrained surgical workspaces while maintaining dexterous mobility presents formidable design hurdles [29], particularly regarding the miniaturization of rigid joints and structural components [30–32].

To address these multifaceted challenges, we introduce an innovative flexible parallel mechanism that synthesizes beneficial attributes from both parallel and continuum robotic paradigms. This design enables adjustable stiffness capability, where low stiffness enhances safety during sensitive procedures such as tissue exploration, whereas high stiffness provides the necessary stability for subsequent surgical manipulations. Our approach transcends conventional design limitations by achieving simultaneous miniaturization and independent stiffness modulation while preserving a functional 1.8 mm central instrument channel. Distinguished from three-branch architectures [33], our six-branch configuration ensures improved load distribution and operational safety through redundant actuation principles. Moreover, our flexible joint implementation obviates the need for complex miniature joints while maintaining positional accuracy.

The principal contributions of this work are as follows. We developed a series-connected flexible parallel mechanism that provides multiple DOFs for motion and stiffness adjustment within a compact form factor incorporating a central instrument channel. We established complete kinematic and stiffness models for this robotic system and validated them through physical prototype implementation. Experimental evaluation demonstrated the system's capabilities in positioning accuracy, load bearing, and operation in constrained environments, confirming its suitability for keyhole surgical procedures.

The remainder of this paper is organized as follows: Section 2 introduces the proposed system and presents its kinematic analysis. Section 3 reports experimental results validating the system's performance. Finally, Section 4 provides a discussion and concluding remarks.

2 | Methods

2.1 | System Description

The robotic system is shown in Figure 1a. The connection between the manipulator and the actuation unit is implemented via a stainless steel tube whose length can be adjusted to suit specific surgical channel constraints. Inside the stainless steel tube are the NiTi rod, inner tube, and outer tube that drive the manipulator. The remaining space accommodates surgical tool drives and other components. Additionally, by integrating master equipment and control algorithms, the completeness of the slave robotic system enables master-slave operation [34, 35].

2.2 | Manipulator With Variable Stiffness Mechanism

The flexible parallel mechanism shown in Figure 1b has the characteristics of dexterity, variable stiffness and high precision. The mechanism consists of two parallel mechanisms connected in series. The remote parallel mechanism consists of 6 NiTi rods with an outer diameter of 0.3 mm. The inherent superelastic properties of the NiTi rod provide commendable capabilities for bending and subsequent recovery [36–38]. Through group actuation of adjacent NiTi rods, the system achieves 2 bending and 1 local translational DOF. The proximal parallel mechanism is composed of 6 flexible inner tubes made of PEEK material, with an outer diameter of 0.8 mm and an inner diameter of 0.4 mm. The NiTi rod of the remote parallel mechanism passes through the inner tube. The spatial structure and driving mode of the proximal parallel mechanism are similar to those of the remote parallel mechanism, with 2 bending DOFs and 1 local translational DOF. Additionally, the robotic has 1 global translational DOF.

Additionally, the structural design of the mechanism is notably compact. Compared to three-branch parallel mechanisms, this six-branch design provides enhanced load distribution and functional redundancy through its 7-DOF architecture, enabling stiffness adjustment while maintaining a fixed pose. This parallel mechanism features multiple branches. Adapting the conventional rigid structure with spherical hinges leads to complex connecting joints, which easily cause deformation and damage under the action of external forces. While system reliability decreases, the difficulty of processing and assembly also increases accordingly [6]. Therefore, we utilize flexible branch chains to replace the rigid links in the mechanism. This approach not only simplifies the kinematic pair but also provides sufficient flexibility and strength for the parallel mechanism. As shown in Figure 1c, the flexible parallel mechanism adopts a nested arrangement of flexible branches. This design facilitates the coaxial arrangement of the driving mechanism and optimizes space utilization for both components. Simultaneously, the structure featuring a central aperture in the manipulator facilitates the convenient driving of surgical tools and the arrangement of sensors.

The parallel mechanism is composed of flexible branch chains with variable lengths, resulting in the stiffness of the mechanism changing with the length of the branch chain. By adjusting the center length of the mechanism, variable stiffness characteristics can be achieved. The manipulator features 5 DOFs for movement and an additional 2 DOFs for stiffness adjustment. This configuration enables not only extensive angle bending and dexterous movement but also stiffness transformation, as shown in Figure 1d.

2.3 | Compact Driver With Linear Motion

The drive mechanism is designed to provide the driving force for manipulator motion control. The manipulator is connected to the drive mechanism using a stainless steel tube with adjustable length. The Bowden Cable principle is employed to transmit the

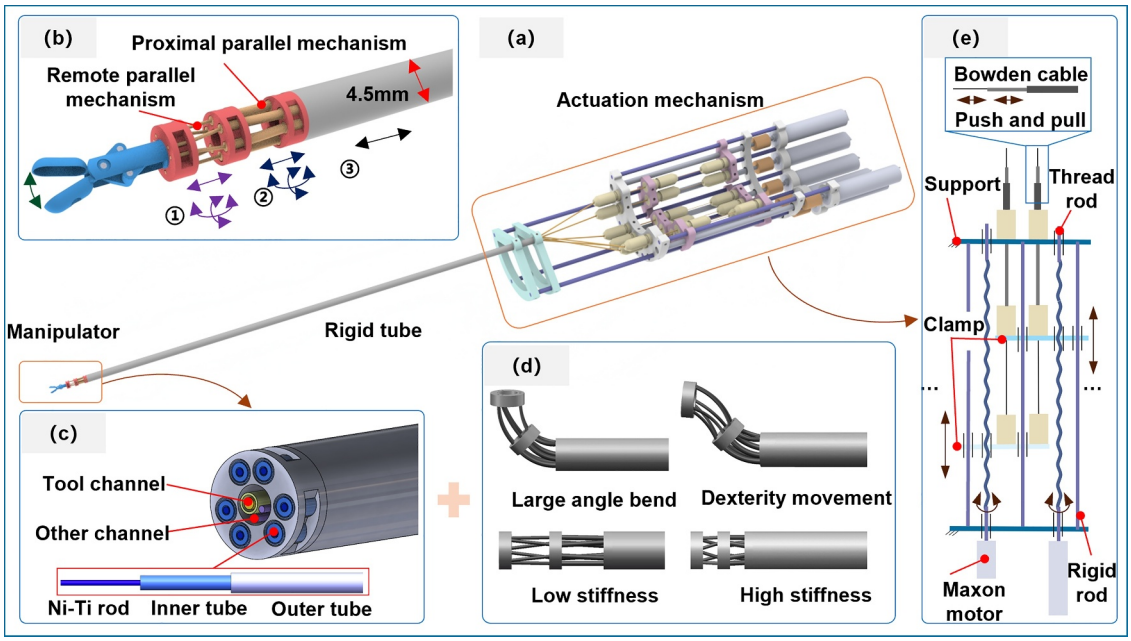

FIGURE 1 | Overview of the robotic system. (a) Details of the robotic system. (b)The flexible parallel manipulator end mechanism. (c) Hole space configuration. (d) Motion characteristics of the manipulator. (e) The connection between the manipulator and the driver system.

motion of the flexible branch chain. Thus, the presence of the inner tube and the outer tube allows the NiTi rod and the inner tube to transmit the linear motion from the driving end. The screw slider is used as the linear motion transmission mechanism, characterized by its compact structure and lightweight. Figure 1e is a schematic diagram of the driving mechanism. Six sliders move axially along the rigid rod, and the motor (DCX13, Maxon, Switzerland) is used to provide power to the robotic system.

2.4 | Kinematic and Workspace Analysis

To simplify the description of the deformation of the coupled elastic rod in this flexible parallel mechanism, we ensure that it moves under conditions of small deformation to maintain the constant curvature of the flexible branch chain bending. The adjacent flexible branch chains of the robotic system are driven simultaneously as a group, and the six branch chains of the parallel mechanism are divided into three groups during the motion modeling process. The kinematic model is shown in Figure 2a,b. The results section validates the model.

The state of the flexible parallel mechanism can be characterized as a virtual parameter $\varphi = [\beta, \delta, L]^T$, connecting the task space to driver space. The position of one segment in the base coordinate can be described as

$$P_{iL}^{ib} = \frac{L}{\beta}\begin{bmatrix} \cos\beta(1-\cos\delta) \\ \sin\beta(1-\cos\delta) \\ \sin\beta \end{bmatrix} \tag{1}$$

Rotation matrix R_{ie}^{ib} associates coordinate $\{2b/2e\}$ and coordinate $\{1b/1e\}$ can be described as

$$R_{ie}^{ib} = R(\hat{z}, \delta)R(\hat{y}, \beta)R(\hat{z}, -\delta) \tag{2}$$

where $R(\hat{z}, \delta)$ represent a rotation by angle δ about axis $\hat{z}$. The transformation matrix coordinate $\{2b/2e\}$ and coordinate $\{1b/1e\}$ can be described as

$$T = \begin{bmatrix} R_{ie}^{ib} & P_{iL}^{ib} \\ 0 & 1 \end{bmatrix} \tag{3}$$

The position of gripper in the world coordinate $\{w\}$ can be described as follows in the robotic manipulator:

$$P_g^w = P_{1b}^w + P_{1L}^{1b} + R_{2b}^{1b}\left(P_{2L}^{2b} + R_{2e}^{2b}P_g^{2e}\right) \tag{4}$$

where P_{1b}^w is the translation from coordinate $\{1b\}$ to world coordinate $\{w\}$ and P_g^{2e} is the gripper tip position in coordinate $\{2e\}$.

In the kinematic model, r_{1i} and r_{2i} denote the bending radii of the i-th driving branch group in the proximal and remote parallel mechanisms, respectively. Considering the relationship between the virtual parameter φ and the driving quantity of each inner tube, the length of each inner tube in the proximal parallel mechanism can be described as

$$l_{1i} = L_1 - r_{1i}\cos\left(\delta_1 + \frac{2\pi}{3}(i-1)\right) \tag{5}$$

Given that the NiTi rod passes through the inner tube, the movement of the proximal parallel mechanism affects the remote parallel mechanism due to coupling. When the proximal parallel mechanism maintains a fixed posture, the length driving amount of the NiTi rod can be described as

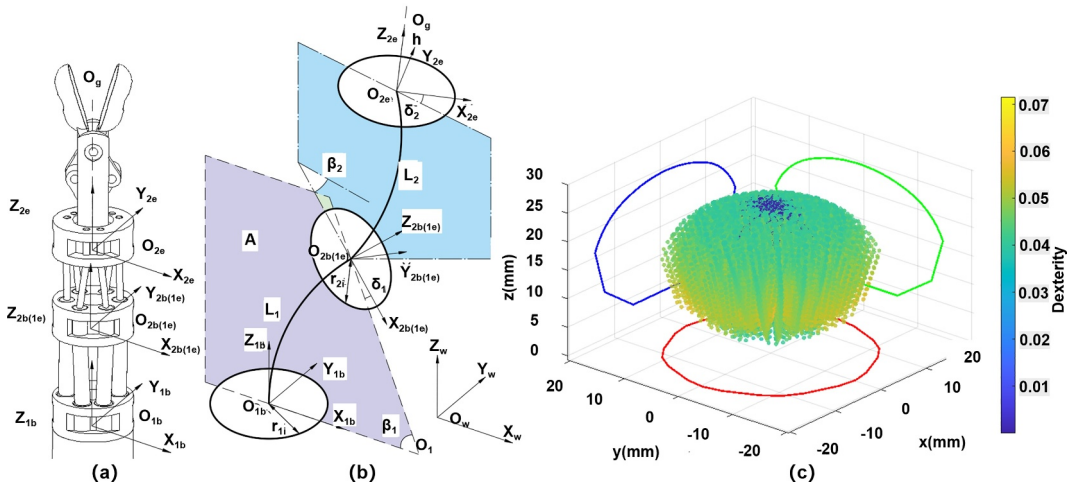

FIGURE 2 | Mechanism kinematic model and simulation analysis. (a) Coordinate system. (b) Kinematic model parameters. (c) Simulated workspace and dexterity based on robotic kinematics.

$$l_{2i} = L_1 - r_{1i}\cos\left(\delta_1 + \frac{2\pi}{3}(i-1)\right) + L_2 - r_{2i}\cos\left(\delta_2 + \frac{2\pi}{3}(i-1)\right) \tag{6}$$

By analyzing the reachable workspace of the surgical robotic and the distribution of operating points in the surgical environment, we can evaluate its feasibility during surgery. Robotic dexterity analysis characterizes the dexterity of robotic operations within the reachable workspace. Surgeons can preplan the surgical area and schedule intricate procedures within regions where the robotic system exhibits high operability [39].

The condition number represents the uniformity of change of the Jacobian transformation matrix in all directions.

$$\kappa_J = \|J_l\|\left\|J_l^{-1}\right\| = \frac{\sigma_{\max}}{\sigma_{\min}} = \sqrt{\frac{\lambda_{\max}}{\lambda_{\min}}} \tag{7}$$

where $\sigma_{\max}$ and $\sigma_{\min}$ represent the maximum and minimum singular values of Jacobian matrix J, $\lambda_{\max}$ and $\lambda_{\min}$ represent the maximum and minimum eigenvalues of matrix JJ^T.

$$\eta_J = \frac{1}{\kappa_J} \epsilon (0, 1] \tag{8}$$

We adopt the reciprocal of the condition number of the Jacobian matrix as the metric to evaluate the dexterity of the manipulator [40, 41]. When the η_J approaches 1, the manipulator is in an isotropic state and has uniform motion ability in all directions. Conversely, when the η_J approaches 0, the manipulator is close to the singular position with the worst motion performance.

The Jacobian matrix can be obtained by taking the derivative of Equation (4).

$$J_{Xq} = \begin{bmatrix} R_{2b}^{1b}\left(J_{2V} - \left[R_{2e}^{2b}P_g^{2e}\right]^{\times} J_{2\omega}\right) & J_{1V} - T_1 J_{1\omega} \\ R_{2b}^{1b} J_{2\omega} & J_{1\omega} \end{bmatrix} \tag{9}$$

where

$$T_1 = \left[R_{2b}^{1b}P_{2L}^{2b} + R_{2e}^{1b}P_g^{2e}\right]^{\times} \tag{10}$$

$[p]^{\times}$ is the skew-symmetric matrix of a vector p.

The reachable workspace of the manipulator is defined as the position set of the target point P_g^w, which is determined by three independent variables of vector q, where q represents the driving variables of the branch chains.

The reachable workspace of a flexible parallel continuum mechanism determines the working range of surgical operations. By using MATLAB simulation software under the condition of each chain length q $\in$ (2 mm, 15 mm), the reachable workspace of the surgical manipulator can be obtained which covers an area of 20 mm × 20 mm × 20 mm, as shown in Figure 2c. In conventional keyhole procedures, such as endoscopic spine surgery, the surgical field typically spans around 20 mm × 20 mm × 30 mm. The designed robotics is capable of moving a distance exceeding 30 mm along the axis. Additionally, the simulation results not only confirm that the reachable workspace of the robotic system satisfies the required criteria but also calculate its operability, offering a valuable reference for the application of the robotic system in minimally invasive surgery.

2.5 | Stiffness Analysis

External force and deformation applied in the surgical tools are $w = \left[F^T, M^T\right]^T$ and $U = \left[\Delta x, \Delta y, \Delta z, \Delta\phi_x, \Delta\phi_y, \Delta\phi_z\right]^T$

Given that each branch chain is connected to the manipulator with fixed joints, the stiffness model of one chain in flexible parallel mechanisms can be expressed as

$$f_i = k_i u_i \tag{11}$$

where k_i is the stiffness matrix of the branch chain [42], which can be described as

$$k_i = \begin{bmatrix} \frac{12EI_2}{l_i^3} & 0 & 0 & 0 & -\frac{6EI_2}{l_i^2} & 0 \\ 0 & \frac{12EI_1}{l_i^3} & 0 & \frac{6EI_1}{l_i^2} & 0 & 0 \\ 0 & 0 & \frac{EA}{l_i} & 0 & 0 & 0 \\ 0 & \frac{6EI_2}{l_i^2} & 0 & \frac{EA}{l_i} & 0 & 0 \\ -\frac{6EI_1}{l_i^2} & 0 & 0 & 0 & \frac{4EI_1}{l_i} & 0 \\ 0 & 0 & 0 & 0 & 0 & \frac{GI_p}{l_i} \end{bmatrix} \tag{12}$$

where E and G represent the Young's modulus and shear modulus of the branch chain, respectively. A and l_i are the cross-sectional area and the effective length, respectively. I_1, I_2, and I_p are the second area moment about the local x-axis and y-axis, and the polar area moment about the local z-axis, respectively.

According to our previous research basis [43], the stiffness of the flexible parallel mechanism can be described as

$$K_u = \sum_{i=1}^{6} \lambda_{u,i}^T k_{u,i} \lambda_{u,i} \tag{13}$$

where $\lambda_{u,i}$ is the deformation compatibility matrix, $k_{u,i}$ is the stiffness matrix of the branch chain.

The equivalent displacement parameter of remote parallel mechanism in coordinate $\{2b\}$ to coordinate $\{1b\}$ can be described as

$$U_2 = w(\mu K_2)^{-1} \tag{14}$$

where

$$\mu = \begin{bmatrix} R^T & -R^T[p]^\times \\ 0 & R^T \end{bmatrix} \tag{15}$$

$[p]^\times$ is the skew-symmetric matrix of a vector p. And

$$\begin{bmatrix} R & p \\ 0 & 1 \end{bmatrix} = R_{2b}^{1b} \tag{16}$$

For the proximal parallel mechanism, the displacement vectors in the coordinate $\{1b\}$ can be described as

$$U_1 = w^{-1} K_1 \tag{17}$$

Combining the displacement of two parallel mechanisms Equations (14) and (17), the equation can be described as

$$w = K(U_1 + \mu U_2) \tag{18}$$

where

$$K = (K_1 + K_2)(K_1 + \mu K_2)^{-1} \tag{19}$$

is the stiffness matrix of the flexible parallel mechanism, K_1 and K_2 are the stiffness matrix of the proximal parallel mechanism and remote parallel mechanism.

3 | Results

3.1 | Accuracy Test

In the realm of keyhole procedures, the precision of master-slave operations is pivotal for guaranteeing surgical efficacy and safety. In order to validate this, the experimental setup was arranged as illustrated in Figure 3a. The setup comprises a surgical robotic, a master hand (Nominal position resolution: ~0.055 *mm*, Sensable Technologies Inc., Woburn, America), an endoscope, and a laser module. Visual feedback during tele-operated tasks is facilitated through endoscopy.

The trajectory plane located within the endoscope's field of view is perpendicular to the manipulator. The surgeon employed the master hand to intuitively and remotely control the tip of the manipulator, guiding it to traverse along the designated trajectory. For visualization and data collection purposes, a laser module is affixed to the tip of the manipulator, emitting a red laser as a marker. The trajectory types cover a wide range of surgical scenarios, including three specifically designed trajectories based on common keyhole procedures. The left column of Figure 3b–d shows Helix, Circular plus, and Pentagram.

For a series of trajectories, the robotic moves forward (depicted by the blue curve) and backward (depicted by the red curve) respectively, as shown in the left column of Figure 3b–d. In our study, we recorded the movement of the laser spot within the endoscopic view and meticulously traced the trajectory based on the red laser using the open-source Physlets Tracker video analysis software.

The series of trajectory error plots in Figure 3b–d shows excellent alignment between the remotely operated trajectory and the reference trajectory. The average errors are as follows: (b) spiral trajectory 0.43 *mm*, with an average speed is 2.02 *mm/s*, (c) Circular plus trajectory 0.52 *mm*, with an average speed is 2.05 *mm/s*, and (d) pentagram trajectory 0.52 *mm*, with an average speed is 1.93 *mm/s*. It is worth noting that larger errors tend to occur during direction changes and arc transitions. This phenomenon is mainly attributed to issues such as hardware clearance and frictional resistance. At the same time, the series of errors in trajectory tracking are closely related to the operator's habits and the theoretical motion model, highlighting the reliability of the theoretical motion model. Furthermore, this observation confirms the high precision of the surgical robotic system in master-slave operations.

3.2 | Test for the Variable Stiffness

The aim of this experiment is to assess the stiffness characteristics of the prototype by inducing deflections at the robotic end and measuring the corresponding reaction force.

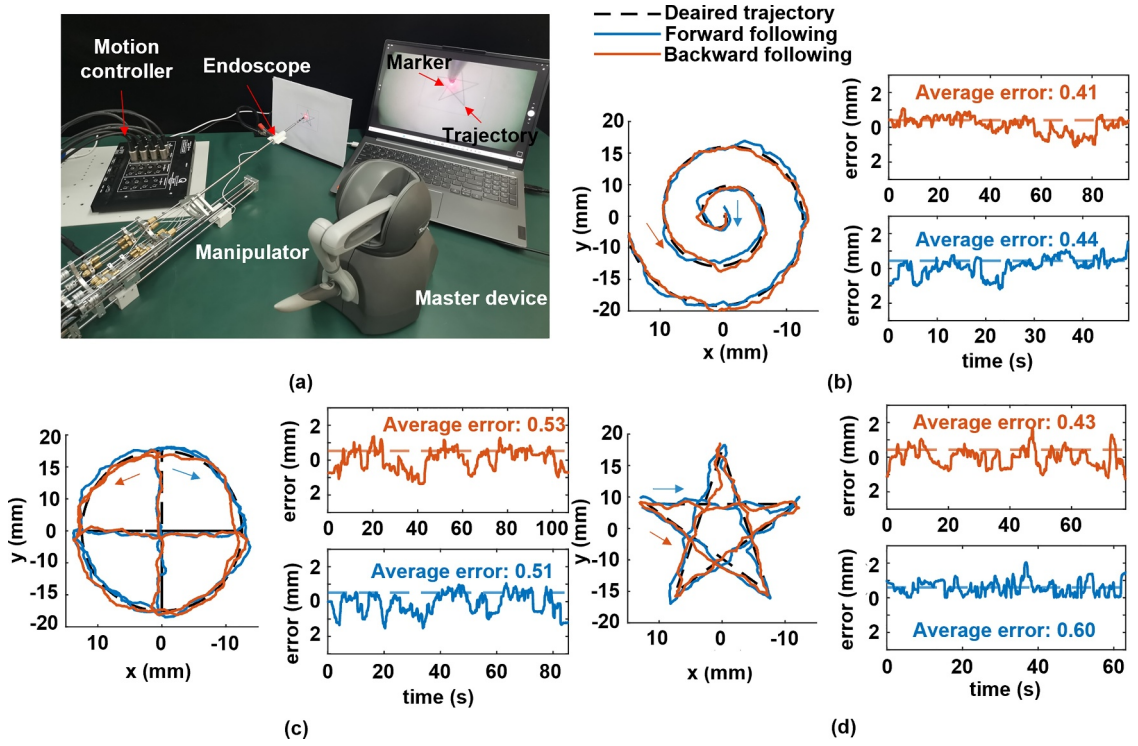

FIGURE 3 | Teleoperation test and error analysis in manipulator movements. (a) Experimental setup with optical tracker and marker. (b) Helix. (c) Circular plus. (d) Pentagram.

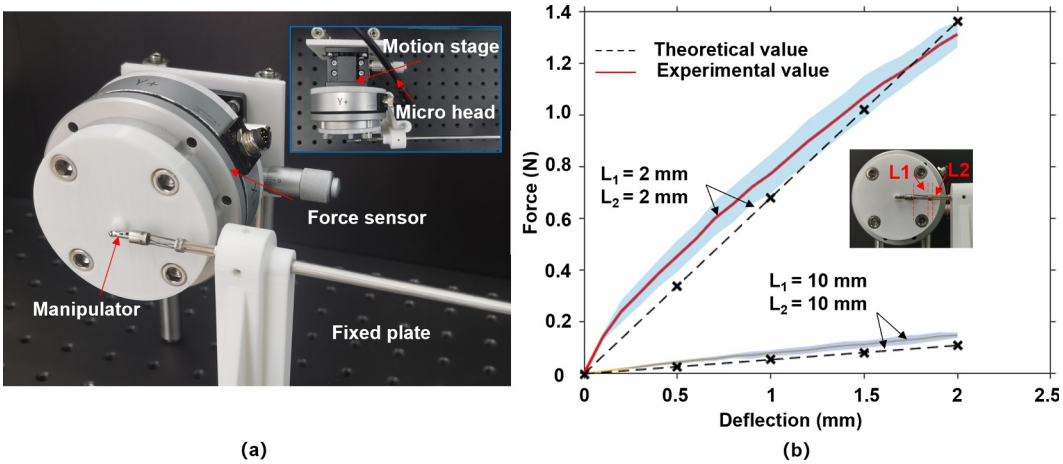

FIGURE 4 | Test for the variable stiffness. (a) Experimental setup of the variable stiffness test. (b) Examine the effect of different lengths of stages on stiffness by fitting the stiffness data of each measuring point.

The experimental device is shown in Figure 4a, including a moving platform and a force sensor (resolution: 15mN, KWR75 A, KUNWEI, China). The manipulator is set as two types of stiffness states with $L_1 = 2\ mm$, $L_2 = 2\ mm$ and $L_1 = 10\ mm$, $L_2 = 10\ mm$. In the above two states, the rotating micro head drives the end of the manipulator to displace 20 times in a direction perpendicular to the central axis of the manipulator in steps of 0.1 mm, and the respective reaction forces are recorded.

Figure 4b characterizes the reaction force against deflection of the manipulator. The dashed curve is the theoretical value calculated by the stiffness model in Section 3. The solid curve represents the average measurement value within the 95% confidence interval of the five test result groups. The measured values closely align with the theoretical values (maximum error: 0.11 N with $L_1 = 2\ mm$, $L_2 = 2\ mm$, 0.04 N with $L_1 = 10\ mm$, $L_2 = 10\ mm$), affirming the accuracy of the stiffness model. With small standard deviations in the measured values, the robotic demonstrates stable performance. The stiffness with $L_1 = 2\ mm$, $L_2 = 2\ mm$ (ranging from 1.26 N/mm to 1.36 N/mm) surpasses that at $L_1 = 10\ mm$, $L_2 = 10\ mm$ (ranging from 0.11 N/mm to 0.16 N/mm), which shows that the stiffness of the manipulator can be effectively adjusted. The observed deviation between theoretical and experimental stiffness values, particularly at shorter mechanism lengths, can be

primarily attributed to two factors. First, the increased influence of friction and internal resistance within the actuation system at higher tension states. Second, the inherent nonlinearity of the material properties under large deformation conditions, which is not fully captured by the linearized model. This suggests that for precise stiffness control in surgical applications, a compensation model accounting for these nonlinear effects would be beneficial.

3.3 | Performance Test

In the keyhole procedures, target areas are spread in multiple directions within tight spaces. Conventional surgical tools struggle with limited flexibility, leading to hard-to-reach areas and poorer results. Therefore, the purpose of this experiment is to selectively harvest green pepper seeds under endoscopy, aiming to evaluate the flexibility of the robotic system during operation. The detailed operation process is shown in Figure 5. The experimental setup consists of a master hand, an endoscopic platform equipped with an adjustable clamp, and a miniature camera with a built-in light source. The miniature camera is firmly positioned at one end of the endoscope platform. A robotic manipulator can navigate into the pepper through the endoscopic platform's tool channel and perform the seed extraction process under the supervision of a tiny camera. The test environment is shown in Figure 5a.

The pepper's inner cavity resembles human body cavities, with seeds sticking to its inner walls (Figure 5b 1). Guided by live endoscopic images, the operator controlled the manipulator to enter the designated area. Subsequently, the surgical robotics controlled to conduct exploratory maneuvers (Figure 5b 2). The forceps were then controlled to collect seeds, which were removed to complete the operation (Figure 5b 3,4). Results demonstrate that the robotic manipulator can access target areas under endoscopic guidance and perform both cavity exploration and seed harvesting effectively, confirming the robotic configuration's functional feasibility.

3.4 | Ex Vivo Test

The surgical environment of keyhole procedures is complex, with mucosa and various tissues distributed within the narrow space. Dexterous operation in tight environments requires compact actuators. Mucus and tissue deformation in the surgical area make surgical operations more difficult. Therefore, in vitro tissue experiments are an important step to further verify the performance of robotics.

As illustrated in Figure 6a, the experimental platform comprises a manipulator, camera, section of chitterlings, and monitor. The robotic instrument and endoscopic unit were guided through separate channels of the simulated platform, with the endoscope delivering video output to the computer monitor.

The motion test was performed inside the chitterlings as shown in Figure 6b,c, including translation, bending, and clamping operations. The operator manipulated the simulated endoscope platform to enter from one end of the large intestine (Figure 6b1,2). The manipulator achieved a smooth linear movement, indicating minimal resistance from the endoscope's internal surface during actuation. Taking the fixed endoscope as a reference, the translation length of the robotic manipulator is greater than 30*mm*. As shown in Figure 6b 3–6, the manipulator achieved bending motion under the restriction of the inner wall, demonstrating that the manipulator possesses adequate torque output to counteract internal structural constraints. And the maximum bending angle is 50°, and the operating radius is greater than 10*mm*. The manipulator can reach multiple locations, demonstrating its dexterity in movement. Figure 6c 1,2 shows that the robot can operate the tissue in the blind area of the field of view in a complex surgical area environment. The distal clamp mechanism functioned reliably even within the spatial limitations of the environment, as shown in Figure 6c 3. All tests confirmed that the designed manipulator possesses exceptional flexibility within the chitterlings, a feature that will be immensely beneficial in future in vivo testing endeavors. While the manipulator demonstrated successful navigation and operation in the simulated environments, its performance revealed important limitations under extreme conditions. The maximum achievable bending angle was reduced when

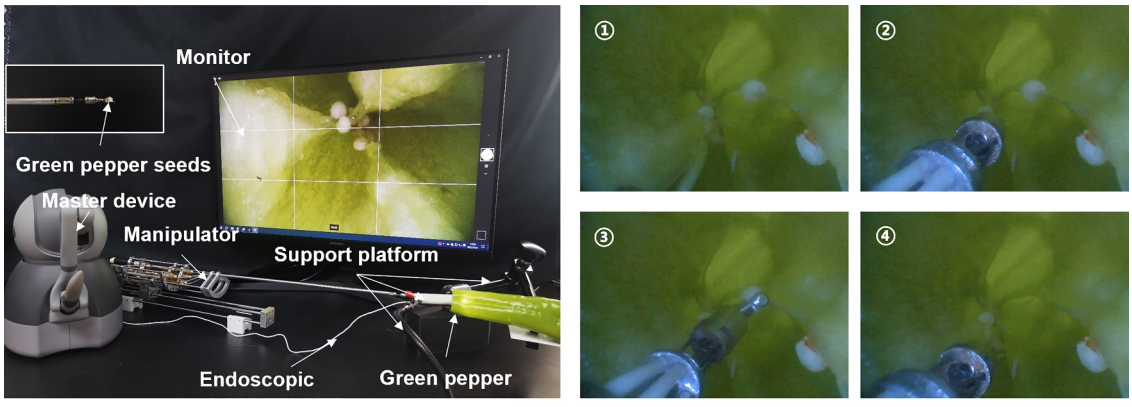

FIGURE 5 | Performance experiment of green pepper seed picking under endoscopic guidance. (a) Depicts the experimental scene layout and the aftermath as the manipulator picks out green pepper seeds and exits. (b) The process of picking green pepper seeds.

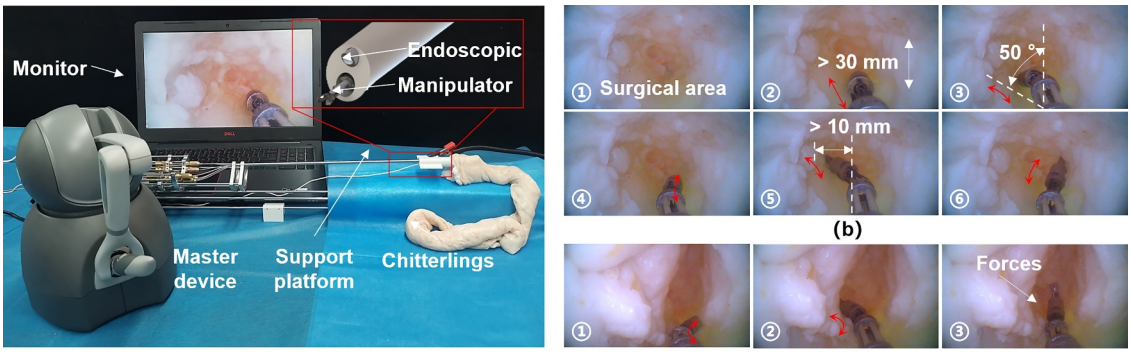

FIGURE 6 | Setup and process of the ex vivo test. (a) Experimental device layout. (b) Manipulator performance test. (c) Surgical operations in complex environments.

operating inside the chitterlings compared to free-space conditions, due to the additional external constraint and friction from the surrounding tissue. This highlights the critical importance of accounting for environmental interactions in future control strategy development for clinical applications.

4 | Discussion and Conclusion

This paper details the mechanical design of a flexible parallel surgical manipulator suitable for keyhole procedures and derives its kinematic and stiffness models. The kinematic performance, variable stiffness capability, and operational flexibility of the robotic system prototype were verified through experiments.

It is worth noting that the parallel mechanism of robotics is composed of flexible branched chains. Compared to the conventional rigid parallel mechanism, the configuration of the mechanism is simplified, reducing the processing difficulty of the hinge and enhancing service life. At the same time, nested branch chains are used to transmit force, and the driving mechanism is concentrically arranged and placed at the rear end, making the structure more compact. In addition, the design also ensures safety and sterilization during the operation of the surgical robotic. Compared with continuum robotics, the design of this flexible parallel mechanism demonstrates excellent operational flexibility and can achieve small bending radius motion with multiple DOFs. In comparison with the cable-driven robotic, this mechanism features a hollow design and incorporates a built-in 1.8 mm instrument channel to accommodate various instrument drive layouts.

In the prototype motion experiment, the designed robotic realized basic motion and tool-driving functions. In the complex narrow lumen, the proximal flexible parallel mechanism can be passively bent and the distal flexible parallel mechanism can move flexibly due to its nested tube drive structure and flexibility. The operator can achieve precise master-slave operation of the robotic within the endoscope's field of view. However, large errors occur when changing the direction of movement due to the presence of manipulator mechanisms and transmission clearance. Additionally, experimental results presented in Section 3.2 demonstrate that the proposed manipulator can achieve significant and controllable stiffness modulation under fixed poses, enabled by the kinematic redundancy of its 7-DOF architecture. This decoupling between stiffness and pose control represents a key advantage for surgical applications, allowing the same configuration to adapt to both delicate exploration and stable manipulation tasks. Considering the minimal curvature of the mechanism in motion and neglecting the influence of slight attitude alterations on stiffness, when the central length of the parallel mechanism remains constant, stiffness remains stable within a specific threshold. In practical motion, the central length of the parallel mechanism is pre-adjusted to align with the required stiffness range. This strategy enables movement at the predetermined length, effectively decoupling stiffness from motion. The variable stiffness capability of the manipulator was verified in the variable stiffness test.

The upcoming research will focus on particular areas of progress. Initially, we will explore mechanics-based kinematic modeling techniques to determine the coupling relationship between motion and stiffness. Secondly, to tackle the issue of restricted visibility in the complex settings of real surgical operations, we are inspired by the capabilities of multi-arm collaborative flexible surgical robotics. Our proposed surgical manipulator will be designed as a modular solution that integrates smoothly with an endoscopic camera and light source, facilitating the flexible maneuvering of the endoscope and thus broadening the visual field.

Author Contributions

Changsheng Li: conceptualization, methodology, validation, supervision, resources, writing – original draft, writing – review and editing, investigation. **Jinpeng Diao:** conceptualization, methodology, validation, writing – original draft, writing – review and editing, visualization. **Chao Qian:** conceptualization, methodology, software, writing – original draft. **Xipeng Wu:** validation, software, writing – review and editing. **Hongliang Ren:** conceptualization, methodology. **Lin Cao:** conceptualization, methodology. **Xingguang Duan:** conceptualization, methodology, resources.

Acknowledgments

This work was supported by the National Key Research and Development Program of China (Grant 2022YFB4703000) and National Natural Science Foundation of China (Grant 62373054).

Funding

This work was supported by the National Key Research and Development Program of China (Grant 2022YFB4703000) and National Natural Science Foundation of China (Grant 62373054).

Conflicts of Interest

The authors declare no conflicts of interest.

Data Availability Statement

The authors have nothing to report.

References

1. O. Alimoglu, J. Sagiroglu, I. Atak, et al., "Robot-Assisted Laparoscopic (RAL) Procedures in General Surgery," *International Journal of Medical Robotics and Computer Assisted Surgery* 12, no. 3 (2016): 427–430, https://doi.org/10.1002/rcs.1706.

2. G. Zhang, J. Su, F. Du, X. Zhang, Y. Li, and R. Song, "Composite Continuum Robots: Accurate Modeling and Model Reduction," *International Journal of Mechanical Sciences* 276 (2024): 109342, https://doi.org/10.1016/j.ijmecsci.2024.109342.

3. Y. Lei, F. Du, H. Song, and L. Zhang, "Design and Kinematics Analysis of a Cable-Stayed Notch Manipulator for Transluminal Endoscopic Surgery," *Biomimetic Intelligence and Robotics* 4 (2024): 100191, https://doi.org/10.1016/j.birob.2024.100191.

4. A. V. Khandge, S. B. Sharma, and J. S. Kim, "The Evolution of Transforaminal Endoscopic Spine Surgery," *World Neurosurgery* 145 (2021): 643–656, https://doi.org/10.1016/j.wneu.2020.08.096.

5. Y. Wang, H. W. Yip, H. Zheng, H. Lin, R. H. Taylor, and K. W. S. Au, "Design and Experimental Validation of a Miniaturized Robotic Tendon-Driven Articulated Surgical Drill for Enhancing Distal Dexterity in Minimally Invasive Spine Fusion," *IEEE* 26, no. 4 (2021): 1858–1866, https://doi.org/10.1109/tmech.2021.3077706.

6. X. Gu and H. Ren, "A Survey of Transoral Robotic Mechanisms: Distal Dexterity, Variable Stiffness, and Triangulation," *Cyborg and Bionic Systems* 4 (2023): 0007, https://doi.org/10.34133/cbsystems.0007.

7. L. Li, X. Li, B. Ouyang, H. Mo, H. Ren, and S. Yang, "Three-Dimensional Collision Avoidance Method for Robot-Assisted Minimally Invasive Surgery," *Cyborg and Bionic Systems* 4 (2023): 0042, https://doi.org/10.34133/cbsystems.0042.

8. Y. Ma, X. An, Q. Yang, et al., "Magnetic Continuum Robot for Intelligent Manipulation in Medical Applications," *SmartBot* 1, no. 2 (2025): e12011, https://doi.org/10.1002/smb2.12011.

9. Y. Peng, X. Liu, K. F. Chan, X. Song, and L. Zhang, "Robotic-Assisted Endovascular Embolization: Progress and Future Perspectives," *SmartBot* 1 (2025): e12009, https://doi.org/10.1002/smb2.12009.

10. J. Kim, M. de Mathelin, K. Ikuta, and D. S. Kwon, "Advancement of Flexible Robot Technologies for Endoluminal Surgeries," in *Proceedings of the IEEE* (IEEE, 2022) 7: 909–931, https://doi.org/10.1109/JPROC.2022.3170109.

11. C. Li, N. K. K. King, and H. Ren, "Preliminary Development of a Skull-Mounted Lightweight Parallel Robot Toward Minimally Invasive Neurosurgery," in *International Symposium on Medical Robotics* (IEEE, 2018), 1–6, https://doi.org/10.1109/ISMR.2018.8333293.

12. K. Oliver-Butler, J. Till, and C. Rucker, "Continuum Robot Stiffness Under External Loads and Prescribed Tendon Displacements," *IEEE Transactions on Robotics* 35, no. 2 (2019): 403–419, https://doi.org/10.1109/tro.2018.2885923.

13. S. A. Pedram, C. Shin, P. W. Ferguson, J. Ma, E. P. Dutson, and J. Rosen, "Autonomous Suturing Framework and Quantification Using a Cable-Driven Surgical Robot," *IEEE Transactions on Robotics* 37, no. 2 (2020): 404–417, https://doi.org/10.1109/tro.2020.3031236.

14. C. Li, Y. Yan, X. Xiao, et al., "A Miniature Manipulator With Variable Stiffness Towards Minimally Invasive Transluminal Endoscopic Surgery," *IEEE Robotics and Automation Letters* 6, no. 3 (2021): 5541–5548, https://doi.org/10.1109/lra.2021.3068115.

15. Z. Li, L. Wu, H. Ren, and H. Yu, "Kinematic Comparison of Surgical Tendon-Driven Manipulators and Concentric Tube Manipulators," *Mechanism and Machine Theory* 107 (2017): 148–165, https://doi.org/10.1016/j.mechmachtheory.2016.09.018.

16. H. Gao, R. Hao, X. Yang, et al., "Modeling and Compensation of Stiffness-Dependent Hysteresis for Stiffness-Tunable Tendon-Sheath Mechanism in Flexible Endoscopic Robots," *IEEE Transactions on Industrial Electronics* 71, no. 8 (2024): 9328–9338, https://doi.org/10.1109/tie.2023.3314891.

17. J. Burgner, D. C. Rucker, H. B. Gilbert, et al., "A Telerobotic System for Transnasal Surgery," *IEEE* 3 (2014): 996–1006, https://doi.org/10.1109/tmech.2013.2265804.

18. W. Li, M. Shen, A. Gao, G. Z. Yang, and B. Lo, "Towards a Snake-like Flexible Robot for Endoscopic Submucosal Dissection," *IEEE Transactions on Medical Robotics and Bionics* 3, no. 1 (2021): 257–260, https://doi.org/10.1109/tmrb.2020.3045507.

19. N. Simaan, A. Kapoor, P. Kazanzides, R. Taylor, and P. Flint, "Design and Integration of a Telerobotic System for Minimally Invasive Surgery of the Throat," *International Journal of Robotics Research* 9 (2009): 1134–1153, https://doi.org/10.1177/0278364908104278.

20. S. Sefati, R. Hegeman, I. Iordachita, R. H. Taylor, and M. Armand, "A Dexterous Robotic System for Autonomous Debridement of Osteolytic Bone Lesions in Confined Spaces: Human Cadaver Studies," *IEEE Transactions on Robotics* 2 (2022): 1213–1229, https://doi.org/10.1109/tro.2021.3091283.

21. S. Lilge, K. Nuelle, J. A. Childs, K. Wen, D. C. Rucker, and J. Burgner-Kahrs, "Parallel-Continuum Robots: A Survey," *IEEE Transactions on Robotics* 40 (2024): 3252–3270, https://doi.org/10.1109/tro.2024.3415230.

22. P. E. Dupont, N. Simaan, H. Choset, and C. Rucker, "Continuum Robots for Medical Interventions,"in *Proceedings of the IEEE*, Institute of Electrical and Electronics Engineers 7 (2022): 847–870, https://doi.org/10.1109/jproc.2022.3141338.

23. C. J. Nwafor, C. Girerd, G. J. Laurent, T. K. Morimoto, and K. Rabenorosoa, "Design and Fabrication of Concentric Tube Robots: A Survey," *IEEE Transactions on Robotics* 4 (2023): 2510–2528, https://doi.org/10.1109/tro.2023.3255512.

24. H. Choi, H. S. Kwak, Y. A. Lim, and H. J. Kim, "Surgical Robot for Single-Incision Laparoscopic Surgery," *IEEE Transactions on Biomedical Engineering* 61, no. 9 (2014): 2458–2466, https://doi.org/10.1109/tbme.2014.2320941.

25. M. Hwang and D. S. Kwon, "Strong Continuum Manipulator for Flexible Endoscopic Surgery," *IEEE* 24, no. 5 (2019): 2193–2203, https://doi.org/10.1109/tmech.2019.2932378.

26. M. S. Saeedi-Hosseiny, F. Alruwaili, S. McMillan, I. Iordachita, and M. H. Abedin-Nasab, "A Surgical Robotic System for Long-Bone Fracture Alignment: Prototyping and Cadaver Study," *IEEE Transactions on Medical Robotics and Bionics* 4, no. 1 (2021): 172–182, https://doi.org/10.1109/tmrb.2021.3129277.

27. M. Leveziel, W. Haouas, G. J. Laurent, M. Gauthier, and R. Dahmouche, "MiGriBot: A Miniature Parallel Robot With Integrated Gripping for High-Throughput Micromanipulation," *Science Robotics* 7, no. 69 (2022): eabn4292, https://doi.org/10.1126/scirobotics.abn4292.

28. M. Zhao, T. J. O. Vrielink, A. A. Kogkas, M. S. Runciman, D. S. Elson, and G. P. Mylonas, "LaryngoTORS: A Novel Cable-Driven Parallel Robotic System for Transoral Laser Phonosurgery," *IEEE Robotics*

and Automation Letters 5, no. 2 (2020): 1516–1523, https://doi.org/10.1109/lra.2020.2969186.

29. J. Diao, C. Qian, X. Xiao, X. Duan, and C. Li, "A Flexible Parallel Robotic Wrist Towards Transluminal Endoscopic Surgery," in *International Conference on Intelligent Robotics and Applications* (Springer, 2023), 420–430, https://doi.org/10.1007/978-981-99-6489-5_34.

30. K. Yan, W. Yan, W. Zeng, et al., "Towards a Wristed Percutaneous Robot With Variable Stiffness for Pericardiocentesis," *IEEE Robotics and Automation Letters* 6, no. 2 (2021): 2993–3000, https://doi.org/10.1109/lra.2021.3062583.

31. Y. J. Kim, S. Cheng, S. Kim, and K. Iagnemma, "A Novel Layer Jamming Mechanism With Tunable Stiffness Capability for Minimally Invasive Surgery," *IEEE Transactions on Robotics* 29, no. 4 (2013): 1031–1042, https://doi.org/10.1109/tro.2013.2256313.

32. Y. Tang, Y. Chi, J. Sun, et al., "Leveraging Elastic Instabilities for Amplified Performance: Spine-Inspired High-Speed and High-Force Soft Robots," *Science Advances* 6, no. 19 (2020): eaaz6912, https://doi.org/10.1126/sciadv.aaz6912.

33. C. Qian, X. Wu, J. Diao, et al., "A Two-Segment 7-DOF Miniature Flexible Parallel Manipulator Toward Minimally Invasive Transluminal Endoscopic Surgery," *IEEE* (2025): 1–11, https://doi.org/10.1109/tmech.2025.3583714.

34. Y. Cai, P. Choi, C. W. V. Hui, R. H. Taylor, and K. W. S. Au, "A Task Space Virtual Fixture Architecture for Teleoperated Surgical System With Slave Joint Limit Constraints," *IEEE* 27, no. 1 (2021): 69–80, https://doi.org/10.1109/tmech.2021.3058174.

35. H. Mo, X. Li, B. Ouyang, G. Fang, and Y. Jia, "Task Autonomy of a Flexible Endoscopic System for Laser-Assisted Surgery," *Cyborg and Bionic Systems* 2022 (2022): 9759504, https://doi.org/10.34133/2022/9759504.

36. M. Jinno and I. Iordachita, "Microgripper Using Flexible Wire Hinge for Robotic Intraocular Snake," in *International Conference on Robotics and Automation* (IEEE, 2022), 6218–6224, https://doi.org/10.1109/ICRA46639.2022.9812022.

37. Y. Hu, L. Zhang, C. A. Seneci, W. Li, M. E. Abdelaziz, and G. Z. Yang, "Design, Fabrication, and Testing a Semiautomatic Sewing Device for Personalized Stent Graft Manufacturing," *IEEE* 24, no. 2 (2019): 517–526, https://doi.org/10.1109/tmech.2019.2894722.

38. C. B. Black, J. Till, and D. C. Rucker, "Parallel Continuum Robots: Modeling, Analysis, and Actuation-Based Force Sensing," *IEEE Transactions on Robotics* 34, no. 1 (2017): 29–47, https://doi.org/10.1109/tro.2017.2753829.

39. J. Burgner-Kahrs, D. C. Rucker, and H. Choset, "Continuum Robots for Medical Applications: A Survey," *IEEE Transactions on Robotics* 31, no. 6 (2015): 1261–1280, https://doi.org/10.1109/tro.2015.2489500.

40. T. Yoshikawa, "Manipulability of Robotic Mechanisms," *International Journal of Robotics Research* 4, no. 2 (1985): 3–9, https://doi.org/10.1177/027836498500400201.

41. C. Gosselin and J. Angeles, "A Global Performance Index for the Kinematic Optimization of Robotic Manipulators," *Journal of Mechanical Design* 113, no. 3 (1991): 220–226, https://doi.org/10.1115/1.2912772.

42. X. Xiao and Y. Li, "Development of an Electromagnetic Actuated Microdisplacement Module," *IEEE* 21, no. 3 (2015): 1252–1261, https://doi.org/10.1109/tmech.2015.2510450.

43. C. Li, X. Gu, X. Xiao, C. M. Lim, and H. Ren, "Flexible Robot With Variable Stiffness in Transoral Surgery," *IEEE* 25 (2019): 1–10, https://doi.org/10.1109/tmech.2019.2945525.